

High-Resolution Laser Spectroscopy on the Hyperfine Structure of ^{255}Fm ($Z=100$)

Mitzi Urquiza-González^{1,2,*} Matou Stemmler,^{3,4} Thomas E. Albrecht,⁵ Benjamin Bally⁶ Michael Bender⁷ Sebastian Berndt,³ Michael Block,^{3,8,9} Alexandre Brizard,^{9,10} Joseph S. Andrews^{9,8} Jacek Bieroń¹¹ Premaditya Chhetri,^{3,8,9} Holger Dorrer,³ Christoph E. Düllmann,^{3,8,9} Julie G. Ezold,¹² Stephane Goriely,¹³ Manuel J. Gutiérrez,^{8,9,14} Dag Hanstorp,¹ Raphael Hasse,³ Reinhard Heinke,¹⁵ Korbinian Hens,² Stephane Hilaire,^{16,17} Magdalena Kaja,³ Tom Kieck,^{8,9} Nina Kneip,^{3,4} Ulli Köster,¹⁸ Andrea T. Loria Basto,^{3,9} Christoph Mokry,^{3,9} Danny Münzberg,^{3,8,9} Kristian Myhre,¹² Thorben Niemeyer,³ Sophie Péru,^{16,17} Sebastian Raeder¹⁵,^{8,9} Dennis Renisch,^{3,8} Jörg Runke,^{3,9} Samantha K. Schrell,¹² Dominik Studer,^{8,9} Kenneth van Beek,^{9,6} Jessica Warbinek,^{3,9} and Klaus Wendt³

¹University of Gothenburg, Gothenburg, Sweden

²Division HÜBNER Photonics, Hübner GmbH & Co KG, Kassel, Germany

³Johannes Gutenberg Universität Mainz, Mainz, Germany

⁴Leibniz University Hannover, Hannover, Germany

⁵Florida State University, Tallahassee, FL, USA

⁶Technische Universität Darmstadt, Darmstadt, Germany

⁷Université Claude Bernard Lyon 1, CNRS/INP2P3,

IP2I Lyon, UMR 5822, F-69100 Villeurbanne, France

⁸Helmholtz-Institut Mainz, Mainz, Germany

⁹GSI Helmholtzzentrum für Schwerionenforschung GmbH, Darmstadt, Germany

¹⁰GANIL, Caen, France

¹¹Uniwersytet Jagielloński, Kraków, Poland

¹²Oak Ridge National Laboratory, Oak Ridge, TN, USA

¹³Université Libre de Bruxelles, Brussels, Belgium

¹⁴Universität Greifswald, Greifswald, Germany

¹⁵CERN, Geneva, Switzerland

¹⁶CEA, DAM, DIF, Arpajon, France

¹⁷Université Paris-Saclay, Bruyères-le-Châtel, France

¹⁸Institut Laue-Langevin, Grenoble, France

(Dated: November 27, 2025)

We report on high-resolution laser spectroscopy of ^{255}Fm ($T_{1/2} = 20\text{h}$), one of the heaviest nuclides available from reactor breeding. The hyperfine structures in two different atomic ground-state transitions at 398.4nm and 398.2nm were probed by in-source laser spectroscopy at the RISIKO mass separator in Mainz, using the PI-LIST high-resolution ion source. Experimental results were combined with hyperfine fields from various atomic *ab-initio* calculations, in particular using MultiConfigurational Dirac-Hartree-Fock theory, as implemented in GRASP18. In this manner, the nuclear magnetic dipole and electric quadrupole moments were derived to be $\mu = -0.75(5)\mu_N$ and $Q_S = +5.84(13)\text{eb}$, respectively. The magnetic moment indicates occupation of the $\nu 7/2[613]$ Nilsson orbital, while the large quadrupole moment confirms strong, stable prolate deformation consistent with systematics in the heavy actinides. Comparisons with available expectation values from nuclear theory show good agreement, providing a stringent benchmark for the used theoretical models. These results revise earlier data and establish ^{255}Fm as a reference isotope for future high-resolution studies.

The radioelement fermium (Fm) with 100 protons in its nucleus is the heaviest element which can be produced in macroscopic amounts. Neutron-capture and nuclear beta-decays of lighter actinide isotopes in nuclear reactors enable the production of pg quantities [1], while heavier elements are produced only in atom-at-a-time quantities [2]. Despite its macroscopic availability, atomic information for fermium is limited [3]. So far, seven optical transitions have been measured with laser spectroscopy [4, 5]. This method can unveil fundamental atomic and nuclear structure properties of nuclides via precision studies of their atomic spectra [6]. In this context, isotope shifts, which give access to changes in the nuclear mean-square charge radii along isotopic chains, were recently

measured in fermium, spanning from ^{245}Fm to ^{257}Fm [7]. Furthermore, investigating the hyperfine structure (HFS) in optical transitions gives access to nuclear moments, which are scarcely known for the heaviest elements, and whose values provide sensitive indicators of underlying shell structure. This fact is visualized in Fig. 1 a), which summarizes the known nuclear dipole moments for nuclides in the region of the heavy actinides. A first attempt to probe the hyperfine structure in a fermium isotope was performed on ^{255}Fm in Ref. [5] with limited resolution and the obtained nuclear dipole moment is reported in the relevant evaluations [8]. As shown in Fig. 1 b) this value for ^{255}Fm deviates from all other known odd-mass (odd-A) nuclide and in fact, it is be-

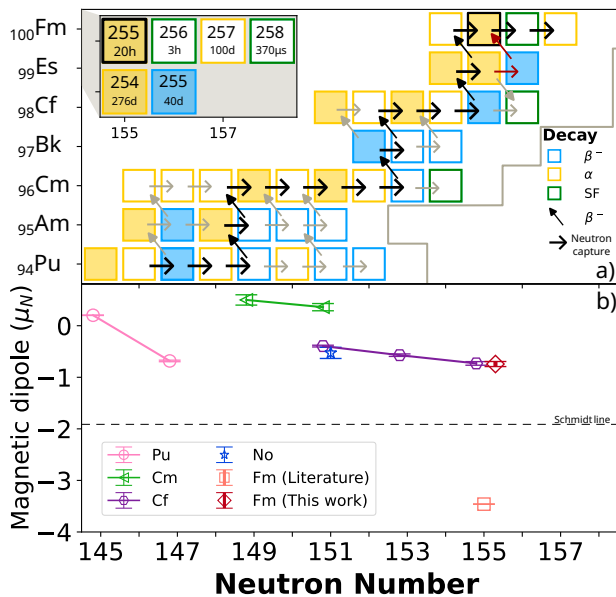


FIG. 1. a) Section of the nuclear chart showing some of the reactor-accessible nuclides [1, 14], including ^{239}Pu . Dark arrows show the primary breeding-path, while light arrows show secondary channels. Red arrows indicate the path taken for this work. Fully colored squares highlight isotopes for which nuclear moments are known. The main decay modes are color-coded following the key given on the right. An insert shows the end of the production pathway, indicating the nuclides' half-lives. b) Magnetic dipole moments of even- Z nuclei ranging from plutonium to nobelium [15–18]. Closely lying values are offset horizontally for visualization.

low the Schmidt line [9, 10] located at $-1.913 \mu_N$ and hence in unphysical space. This line is derived from a simplified single-particle shell model that assumes that the total nuclear magnetic moment equals the moment of its single unpaired nucleon [11]. To further elucidate this situation, we investigated the hyperfine splitting of atomic transitions in ^{255}Fm with high resolution using the perpendicularly-illuminated laser ion source and trap (PI-LIST) [12] at the RISIKO mass separator [13]. From the experimentally extracted hyperfine coupling constants, the nuclear magnetic dipole and electric quadrupole moments were determined by combining the experimental results with dedicated atomic and nuclear calculations, providing an updated and reliable reference for the nuclear moments.

The measurements were performed on several samples of ^{255}Fm , each containing 10^8 to 10^9 atoms. These were produced from an initial sample of $8.8 \cdot 10^{13}$ atoms of ^{254}Es , equivalent to 34 ng, provided by Oak Ridge National Laboratory (ORNL) and Florida State University, Tallahassee, USA [1]. This initial sample was neutron irradiated in the high-flux research reactor at the Institut Laue-Langevin (ILL) in Grenoble, France for 7 days. After a cooling period of 4 days, the sample was transported to the Johannes Gutenberg University, Mainz,

Germany. $7.5 \cdot 10^{10}$ atoms of ^{255}Es ($T_{1/2} = 39.8$ d) [15] were available to be used as a $^{255}\text{Es}/^{255}\text{Fm}$ generator. This production path is depicted in red in Fig. 1. At the Department of Chemistry – TRIGA site at Mainz, on-site chemical separations were performed using a cation-exchange column chromatography technique with alpha-hydroxyisobutyrate as the eluting agent [7]. The fermium fraction was then placed on a zirconium foil and evaporated to dryness. This on-site separation allowed performing an extended measuring campaign by yielding multiple samples at timed intervals after secular equilibrium was established between individual separations.

At the RISIKO mass separator [13], neutral fermium atoms were produced by placing a sample in the atomizer and resistively heating it to a typical temperature of 900°C [13]. All laser excitations took place within the PI-LIST structure [12, 20], which consists of two repelling electrodes, installed immediately in front of the atomizer, and a radio frequency quadrupole (RFQ) ion guide. Within the RFQ structure, just a few millimeters apart from the front of the atomizer, the effused neutrals are intersected by the first laser beam. The spectroscopy (first step) laser is arranged in a perpendicular geometry and the ionization (second step) laser in an anti-collinear configuration relative to the effusing atomic beam. The overlap of both lasers with each other and the atomic beam defines and limits the effective aperture angle of the atomic beam. This enables a narrow velocity spread with respect to the spectroscopy laser, reducing the Doppler broadening to approximately 50 MHz in the first step.

Ions created inside the RFQ structure were extracted through the PI-LIST's exit electrodes and accelerated to 30 keV. They were then mass separated in a 60° -sector-field dipole magnet according to their mass-to-charge ratio with a typical resolving power of $M/\Delta M \simeq 600$. Finally, ions were counted on a secondary electron multiplier (SEM) for single ion detection. By using pulsed lasers, a bunch structure was imprinted on the detected ions and a time-resolved acquisition further reduced the background, using a multichannel analyzer and gating to the bunch structure of 20–30 μs duration.

Two pulsed titanium:sapphire (Ti:sapphire) laser systems provided the photons to drive two resonant transitions from the ground-state (GS), historically [4, 5] named *Resonance 1* (R1) at $25\,099\text{ cm}^{-1}$ and *Resonance 2* (R2) at $25\,111\text{ cm}^{-1}$, to the corresponding intermediate levels at the respective wavelengths as given in Fig. 2. The narrow-bandwidth laser light of the first step was generated with an injection-locked Ti:sapphire laser [21] and single-pass second harmonic generation (SHG), with typical average laser powers of 20 mW in the PI-LIST interaction area. The typical spectral characteristics of this system were close to Fourier-limited bandwidths of 20 MHz in the fundamental [21] while the scanning range was defined by a continuous wave (cw) master laser. To ease operation, a diode laser (TOPTICA, DL PRO) was used as master

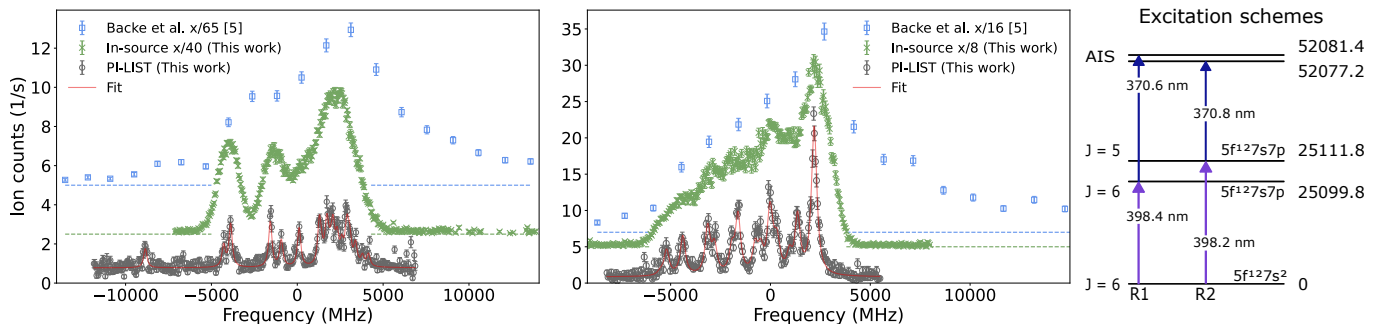


FIG. 2. Measured HFS spectra for in-source spectroscopy (green) and with the PI-LIST (gray) together with results from Backe et al. [5]. For greater clarity, the spectra have an individual vertical offset (dashed lines). Left: spectra for R1 relative to the energy of 25 099.760(14) cm^{-1} . Center: spectra for R2 centered relative to the centroid energy of 25 111.760(12) cm^{-1} . On the right, the excitation schemes and the auto-ionizing states (AIS) used in this work are shown, along with their energies expressed in wavenumbers (cm^{-1}). The atomic configurations of the GS and excited states are also indicated [19].

laser for R1, while for R2 a diode pumped cw-Ti:sapphire [22] was chosen. The ionizing pulses were generated by an in-house-built high-power Ti:sapphire laser with two gain crystals, providing 1.3 W of laser light entering the vacuum chamber after SHG. The spectral, spatial, and temporal beam qualities were similar to those of a standard Ti:sapphire laser [23]. Both systems were driven by individual pump lasers at 532 nm with a repetition rate of 10 kHz, synchronized by an external pulse-pattern generator. The fundamental wavelength of both laser systems was constantly measured by a wavemeter (HighFinesse WSU30) with a nominal absolute accuracy of 30 MHz, which was periodically calibrated to a well-known rubidium transition [24]. Similar setups have been previously used for high-resolution spectroscopy of several elements [16, 17, 20, 25, 26].

Recorded spectra in ^{255}Fm for the transitions R1 and R2 are shown in Fig. 2. To ensure high efficiency, an initial signal was generated with the first-step laser in anti-collinear geometry, directly ionizing in-source. In this way, the first spectra were taken with limited spectral resolution due to the Doppler broadening, shown in green. The narrow-bandwidth first-step laser was then aligned perpendicularly in the PI-LIST, while being repeatedly scanned across the resonance structure, maintaining a substantially low but nearly constant atomic-beam current. These spectra, binned with 50 MHz, are shown in gray, with the majority of the hyperfine components being well resolved and their best fit shown in red. Blue data points show data from Backe et al. [5] obtained from spectroscopy in a buffer gas cell. Here the spectral resolution was mostly limited by a strong Doppler broadening, pressure broadening, and a large laser bandwidth.

As the angular momentum J of the atomic shell is larger than the nuclear spin $I = 7/2$, each atomic state splits into $2I + 1 = 8$ HFS levels. With the achieved experimental resolution and efficiency, 15 out of 22 expected components were observed for R1 and 13 out of 21 for R2, while the remaining components were not fully

resolved. Nevertheless, the large redundancy in the structure allows extracting the hyperfine parameters with high precision. A HFS model was fitted to the binned data using Satlas2 [27], knowing that the HFS energy splitting of an atomic level is given by

$$\Delta\nu = \mathcal{A} \cdot \frac{C}{2} + \mathcal{B} \cdot \frac{3C(C+1) - 4I(I+1)J(J+1)}{8I(2I-1)J(2J-1)}, \quad (1)$$

where \mathcal{A} and \mathcal{B} are the HFS coupling constants, and the Casimir factor $C = F(F+1) - I(I+1) - J(J+1)$, where F is the total angular momentum. Derived from the electronic angular momentum (J) and nuclear spin (I), Racah intensities were calculated to determine relative strengths of the HFS components. Accordingly, fixed intensity ratios to close-lying poorly resolved peaks were assigned while the intensities of the fully-resolved components were set as free parameters to account for optical hyperfine pumping contributions and variations of the atom source conditions. Since the GS HFS coupling constants are the same for both transitions, these were shared between the two fitting models for a more precise result [28].

The angular momentum J of each respective excited state was also investigated, as a definite value had not been given before [5]. As other assignments did not result in any convergence and did not lead to a reasonable reproduction of either HFS spectra, this work confirms the values for the excited levels $J_{R1e} = 6$ and $J_{R2e} = 5$ and thus, confirms the assignment to the levels given by Allehabi et al. [19]. A linewidth of 230 MHz (350 MHz) was extracted for R1 (R2), mostly dominated by power broadening, resulting from the compromise between resolution and efficiency. Taken from the best fit to the data as shown in Fig. 2, the extracted HFS coupling constants are summarized in Table I where the GS values result from the shared fit model. Our results clearly differ from the values given in Ref. [5], which were negatively affected by the low resolution and the presence of an unresolvable high-energy tail in their spectra, likely caused

TABLE I. Experimentally extracted HFS coupling constants for ^{255}Fm for each studied atomic energy level. R1_e and R2_e represent the first excited level for R1 and R2, respectively. An error of 50% was estimated by Backe et al. [5].

State	J	\mathcal{A} [GHz]		\mathcal{B} [GHz]	
		This work	Backe et al.	This work	Backe et al.
GS	6	-0.1495(11)	-0.32	-10.46(4)	-22
R1 _e	6	-0.3092(12)	-0.53	-12.79(4)	-2.9
R2 _e	5	-0.0097(13)	-0.69	-13.57(5)	-1.7

by their dye lasers' spectral profile. The high resolution of the PI-LIST spectra and the application in different geometries removes any ambiguity and revises these values with a significantly improved precision.

Uncertainties were determined from statistical distribution of the ion counts and the systematic uncertainty inherent to the wavemeter, determined by modulating the experimental data with a triangle function with arbitrary phase as suggested in Ref. [24]. In addition, the dependence of the extracted results to the binning was investigated and found to be well within the extracted uncertainty range. As a cross check, the Doppler-broadened data were included in the fitting routine, resulting in a full agreement without significant influence on the final HFS values and their uncertainties.

To extract the magnetic dipole moment μ and the spectroscopic electric quadrupole moment Q_S , the knowledge of the hyperfine fields is needed. In the case of fermium, with no stable reference isotope aiding to fix atomic quantities with standard techniques, the magnetic field at the nucleus ($B_e(0)$) and the electric-field gradient of the electronic cloud at the site of the nucleus ($\langle \partial^2 V / \partial z^2 \rangle_{z=0}$) have to be taken from accurate atomic theory calculations [3, 6]. On the basis of the experimentally extracted values for \mathcal{A} and \mathcal{B} using equation 1, we obtain the nuclear moments for ^{255}Fm from the relation

$$\mathcal{A} = \mu_I \frac{B_e(0)}{IJ} \quad \text{and} \quad \mathcal{B} = eQ_S \left\langle \frac{\partial^2 V}{\partial z^2} \right\rangle_{z=0}. \quad (2)$$

The hyperfine fields in equation 2 can also be equated for HFS coupling constants measured in different isotopes, enabling the derivation of nuclear moments if they are known for at least one isotope.

Despite the open f -shell character of fermium, recent atomic calculations using the configuration interaction with perturbation theory (CIPT) method predicted some neutral atomic level scheme along with hyperfine fields [19, 29]. To evaluate the reproducibility of these fields across different theoretical approaches, dedicated MultiConfigurational Dirac-Hartree-Fock (MCDHF) calculations were performed within this work. The use of the MCDHF theory as implemented in GRASP18 [30] is described in Appendix A. Table II summarizes these results,

TABLE II. Theoretical atomic calculations for the ground-state $[\text{Rn}] 7s^2 5f^{12} 3H_6$ hyperfine fields \mathcal{A}/g_i and \mathcal{B}/Q_S from CIPT and MCDHF theory. The values for the \mathcal{A} -factor are given in a nuclear spin-independent notation with respect to the g_i -factor with $g_i \cdot I = \mu_I$. Uncertainties are given only for the calculations done for this work. The average values are taken from all calculations and the uncertainties are their associated standard deviations [33, 34].

Method	\mathcal{A}/g_i [GHz/ g_i]	\mathcal{B}/Q_S [GHz/ eb]
CIPT [19]	0.655	-1.750
CIPT [29]	0.759	-1.844
MCDHF [32]	0.725	-1.782
MCDHF (This work)	0.694	-1.789
Average	0.708(44)	-1.791(39)

including available results from calculations using CIPT methods as reported in Refs. [19] and [31], a previous MCDHF calculation reported by Ref. [32], and the new MCDHF results obtained in this work. As the values show a very good agreement across the different calculations and different theoretical frameworks, the average value is taken for the extraction of nuclear parameters and its uncertainty calculated from the standard deviation of all four methods [33, 34].

For the excited states R1 and R2 in the CIPT calculations [19, 29], Dzuba et al. [29] declare that *"the state R2 has [an] anomalously small value of \mathcal{A} . This means that the theoretical uncertainty for this state is large and the state is not very good for the extraction of nuclear parameters."* This is very much in agreement with our experimental findings and MCDHF results, indicating discrepancies and no convergence for either state. Thus, only the GS values are used further.

The combination of the experimental results from Table I and the atomic calculations from Table II enabled the extraction of nuclear moments for ^{255}Fm as given in Table III. Here the magnetic dipole moment $\mu_I(^{255}\text{Fm}) = -0.743(49) \mu_N$ is well within the Schmidt limit [9], in contrast to the evaluation performed with the unresolved spectra in Ref. [5].

To gain more insight, these results are compared with predictions obtained from two microscopic nuclear models based on the energy density functional framework. The first model is using the Gogny force D1M [35] and consists in Hartree-Fock-Bogoliubov (HFB) calculations supplemented by approximate beyond-mean-field corrections [33, 36]. The second model is using the Skyrme SLyMR1 interaction [37, 38] and performs a full configuration mixing of symmetry-restored triaxial reference states within a Multi-Reference Energy Density Functional (MREDF) approach [39, 40]. Details about the models can be found in Appendix B. We remark that both models also describe the evolution of isotopic shifts of charge radii of fermium isotopes reasonably well [7].

These nuclear calculations agree very well with the

TABLE III. Extracted experimental nuclear parameters for ^{255}Fm in comparison to nuclear calculations (bold). The theoretical calculations cover further odd fermium isotopes and isomers, as indicated. Tentative ground state spin assignments (indicated by parentheses) are used to infer the level from the nuclear calculations.

Isotope	I/\hbar	Method	μ/μ_N	Q_S/eb
^{255}Fm	7/2	Experiment	-0.743(49)	5.84(13)
^{257}Fm	(9/2)	MREDF	1.7	7.7
^{255}Fm	7/2	MREDF	-1.0	6.2
^{257}Fm	(9/2)	HFB	1.4	6.67
^{255}Fm	7/2	HFB	-0.78	5.78
^{253}Fm	1/2	HFB	-1.047	0
^{251}Fm	(9/2)	HFB	-0.730	7.06
^{249}Fm	(7/2)	HFB	1.215	6.01
^{247g}Fm	(7/2)	HFB	1.211	5.99
^{247m}Fm	(1/2)	HFB	0.363	0
^{245}Fm	(1/2)	HFB	0.355	0

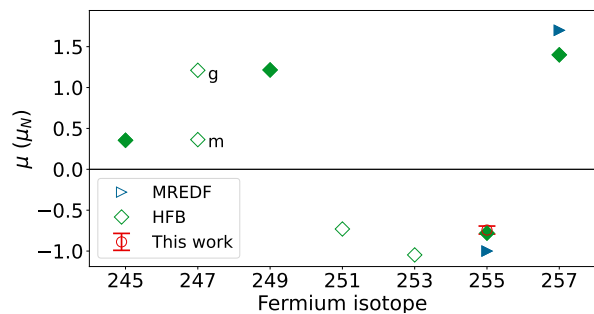


FIG. 3. Predicted and experimental magnetic moments for some fermium isotopes. Common isotopes also included in Ref. [7] are marked as solid symbols.

experimental results as summarized in Table III. The MREDF calculations overestimate the nuclear magnetic dipole moment by approximately 25% and the electric quadrupole moment by around 6%, whereas the deviation from the HFB results remains below 5% in both cases. In addition, the nuclear moments of ^{255}Fm closely match the values of the isotone even-odd nucleus ^{253}Cf with $\mu_I(^{253}\text{Cf}) = -0.731(35) \mu_N$ and $Q_S(^{253}\text{Cf}) = 5.53(51) eb$ [17]. This indicates that the same neutron valence orbital is occupied in both nuclei, suggested to be the $\nu 7/2[613]$ Nilsson orbital for ^{253}Cf [8]. This orbital is then also expected to be involved in the odd-odd nucleus ^{254}Es , where it couples with the $\pi 7/2[633]$ orbital (valence proton in $^{253,255}\text{Es}$) in a full alignment to a total spin of $I_{254\text{Es}} = 7$ [16]. Within their uncertainty, the quadrupole moments are also identical between ^{255}Fm and ^{253}Cf , which is expected in this region of stable, strongly prolate deformed nuclei where experimental charge radii did not reveal any change in shape [7].

Based on these nuclear structure calculations, in Fig. 3, we further provide predictions for the magnetic dipole

moment of the ground state of neighboring fermium isotopes where experimental results from high-resolution laser spectroscopy are not yet available. However, several isotopes were studied with reduced resolution recently by Warbinek et al. [7]. As the total width of the HFS is determined by the magnetic dipole moment, a qualitative comparison can be made with these results. From their appendix section, the HFS of ^{257}Fm is clearly wider than that of ^{245}Fm , which is in agreement with the prediction made by the HFB calculations.

In this Letter we have reported on the first high-resolution spectra of an atomic transition in the isotope ^{255}Fm , using the PI-LIST at the RISIKO mass separator, with samples of around 10^8 atoms. This enabled probing the HFS of atomic transitions, previously only observed unresolved [4, 5]. In combination with reported and newly calculated atomic coupling constants from atomic theory the nuclear magnetic dipole moment $\mu_I(^{255}\text{Fm}) = -0.75(5) \mu_N$ and the nuclear electric quadrupole moment $Q_S(^{255}\text{Fm}) = +5.84(13) eb$ were determined. These results were compared to predictions from nuclear MREDF and HFB calculations, which are in good agreement for ^{255}Fm . The nuclear theory calculations covered additional odd-A fermium isotopes, some of which have previously been studied in on-line experiments with limited resolution [7]. Improved experimental results appear within reach, e.g., from future upgrades of the JetRIS apparatus at GSI Darmstadt [41] and the upcoming S^3 low-energy-branch at GANIL, France [42]. ^{255}Fm now serves for the prediction of expected HFS and is available as a reference isotope.

Acknowledgments — We thank the mechanical workshop and radiation protection staff at TRIGA Mainz and R. Jera, glassblower at JGU Chemistry, the ILL reactor and health physics teams, and N. Sims, radioisotope laboratory technician at ORNL. The isotopes used in this research were supplied by the U.S. Department of Energy, Office of Science, Isotope R&D and Production program. This research was supported by the U.S. Department of Energy Office of Science, Office of Basic Energy Sciences, Heavy Element Chemistry program under Award Number DE-SC0023693. The $^{253,254,255}\text{Es}$ was provided to Florida State University via the Isotope Development and Production for Research and Applications Program through the Radiochemical Engineering and Development Center at ORNL. S.G. acknowledges financial support from F.R.S.-FNRS (Belgium). This work has received funding from the German Bundesministerium für Bildung und Forschung under Project No. 05P21UMFN3, 05P15RDFN1 and 05P21RDFN1; from the Swedish Research Council under Grant No. 2024-04152; from the European Research Council under the European Union’s Horizon 2020 Research and Innovation Programme (Grant Agreement No. 819957) and Horizon Europe Research and Innovation Programme (Grant Agreement No. 101162059). This Marie Skłodowska-

Curie Action Innovative Training Networks received funding from the European Union's H2020 Framework Programme under grant agreement No. 861198.

* Contact author: mitzi.urquiza@gu.se

- [1] J. Roberto, C. Alexander, R. Boll, J. Burns, J. Ezold, L. Felker, S. Hogle, and K. Rykaczewski, Actinide targets for the synthesis of super-heavy elements, *Nuclear Physics A* **944**, 99 (2015), special Issue on Superheavy Elements.
- [2] O. R. Smits, Ch. E. Düllmann, P. Indelicato, W. Nazarewicz, and P. Schwerdtfeger, The quest for superheavy elements and the limit of the periodic table, *Nat. Rev. Phys* **6**, 86 (2024).
- [3] M. Block, M. Laatiaoui, and S. Raeder, Recent progress in laser spectroscopy of the actinides, *Progress in Particle and Nuclear Physics* **116**, 103834 (2021).
- [4] M. Sewtz, H. Backe, A. Dretzke, G. Kube, W. Lauth, P. Schwamb, K. Eberhardt, C. Grüning, P. Thörle, N. Trautmann, *et al.*, First observation of atomic levels for the element fermium ($Z = 100$), *Phys. Rev. Lett.* **90**, 163002 (2003).
- [5] H. Backe, A. Dretzke, S. Fritzsche, R. G. Haire, P. Kunz, W. Lauth, M. Sewtz, and N. Trautmann, Laser Spectroscopic Investigation of the Element Fermium ($Z = 100$), *Hyperfine Interact.* **162**, 3 (2005).
- [6] X. Yang, S. Wang, S. Wilkins, and R. G. Ruiz, Laser spectroscopy for the study of exotic nuclei, *Progress in Particle and Nuclear Physics* **129**, 104005 (2023).
- [7] J. Warbinek, E. Rickert, S. Raeder, *et al.*, Smooth trends in fermium charge radii and the impact of shell effects, *Nature* **634**, 1075–1079 (2024).
- [8] E. Browne and J. Tuli, Nuclear Data Sheets for $A = 251$ – 259 (odd), *Nucl. Data Sheets* **114**, 1041 (2013).
- [9] T. Schmidt, Über die magnetischen Momente der Atomkerne, *Zeitschrift für Physik* **106**, 358 (1937).
- [10] K. S. Krane and D. Halliday, *Introductory nuclear physics* (Wiley, New York, 1987).
- [11] R. P. de Groote and G. Neyens, Spins and Electromagnetic Moments of Nuclei, in *Handbook of Nuclear Physics*, edited by I. Tanihata, H. Toki, and T. Kajino (Springer Nature Singapore, Singapore, 2020) pp. 1–36.
- [12] R. Heinke, T. Kron, S. Raeder, T. Reich, P. Schönberg, M. Trümper, C. Weichhold, and K. Wendt, High-resolution in-source laser spectroscopy in perpendicular geometry, *Hyperfine Interact.* **238**, 6 (2016).
- [13] T. Kieck, H. Dorrer, Ch. E. Düllmann, V. Gadelshin, F. Schneider, and K. Wendt, Highly efficient isotope separation and ion implantation of ^{163}Ho for the ECHO project, *Nucl. Instrum. Methods Phys. Res.* **945**, 162602 (2019).
- [14] S. Hogle, J. G. Ezold, and C. Alexander, Californium-252 production in the high flux isotope reactor (2013), test Research and Training Reactors 2013 Annual Conference.
- [15] F. Kondev, M. Wang, W. Huang, S. Naimi, and G. Audi, The NUBASE2020 evaluation of nuclear physics properties, *Chinese Physics C* **45**, 030001 (2021).
- [16] S. Nothhelfer *et al.*, Nuclear structure investigations of 253 – ^{255}Es by laser spectroscopy, *Phys. Rev. C* **105**, L021302 (2022).
- [17] F. Weber *et al.*, Nuclear moments and isotope shifts of the actinide isotopes 249 – ^{253}Cf probed by laser spectroscopy, *Phys. Rev. C* **107**, 034313 (2023).
- [18] S. Raeder, D. Ackermann, H. Backe, R. Beerwerth, J. C. Berengut, M. Block, A. Borschevsky, B. Cheal, P. Chhetri, Ch. E. Düllmann, V. A. Dzuba, E. Eliav, J. Even, R. Ferrer, V. V. Flambaum, S. Fritzsche, F. Giacoppo, S. Götz, F. P. Heßberger, M. Huyse, U. Kaldor, O. Kaleja, J. Khuyagbaatar, P. Kunz, M. Laatiaoui, F. Lautenschläger, W. Lauth, A. K. Mistry, E. Minaya Ramirez, W. Nazarewicz, S. G. Porsev, M. S. Safronova, U. I. Safronova, B. Schuetrumpf, P. Van Duppen, Th. Walther, C. Wraith, and A. Yakushev, Probing sizes and shapes of nobelium isotopes by laser spectroscopy, *Phys. Rev. Lett.* **120**, 232503 (2018).
- [19] S. O. Allehabi, J. Li, V. Dzuba, and V. Flambaum, Theoretical study of electronic structure of erbium and fermium, *J. Quant. Spectrosc. Radiat. Transfer* **253**, 107137 (2020).
- [20] T. Kron, R. Beerwerth, S. Raeder, S. Fritzsche, R. Heinke, P. Schönberg, M. Trümper, and K. Wendt, Hyperfine structure study of $^{97,98,99}\text{Tc}$ in a new laser ion source for high-resolution laser spectroscopy, *Phys. Rev. C* **102**, 034307 (2020).
- [21] V. Sonnenschein, I. D. Moore, S. Raeder, M. Reponen, H. Tomita, and K. Wendt, Characterization of a pulsed injection-locked Ti:sapphire laser and its application to high resolution resonance ionization spectroscopy of copper, *Laser Phys.* **27**, 085701 (2017).
- [22] V. Sonnenschein, M. Ohashi, H. Tomita, and T. Iguchi, A direct diode pumped continuous-wave Ti:sapphire laser as seed of a pulsed amplifier for high-resolution resonance ionization spectroscopy, *Nuclear Instruments and Methods in Physics Research Section B: Beam Interactions with Materials and Atoms* **463**, 512 (2020).
- [23] C. Mattolat, S. Rothe, F. Schwellnus, T. Gottwald, S. Raeder, and K. Wendt, An all-solid-state high repetition rate titanium:sapphire laser system for resonance ionization laser ion sources, in *AIP Conference Proceedings*, Vol. 1104 (2009) pp. 114–119.
- [24] M. Verlinde, K. Dockx, S. Geldhof, K. König, D. Studer, *et al.*, On the performance of wavelength meters: Part 1—consequences for medium-to-high-resolution laser spectroscopy, *Applied Physics B* **126**, 85 (2020).
- [25] M. Kaja, M. Urquiza-González, F. Berg, T. Reich, M. Stemmler, D. Studer, F. Weber, and K. Wendt, High-resolution laser spectroscopy on the hyperfine structure and isotope shift of $^{237,239}\text{Np}$, *The European Physical Journal A* **60**, 140 (2024).
- [26] D. Studer, J. Ulrich, S. Braccini, T. S. Carzaniga, R. Dressler, K. Eberhardt, R. Heinke, U. Köster, S. Raeder, and K. Wendt, High-resolution laser resonance ionization spectroscopy of 143 – ^{147}Pm , *The European Physical Journal A* **56**, 69 (2020).
- [27] W. Gins, B. van den Borne, R. de Groote, and G. Neyens, SATLAS2: An update to the package for analysis of counting data, *Comput. Phys. Commun* **297**, 109053 (2024).
- [28] W. Gins, R. de Groote, M. Bissell, C. Granados Buitrago, R. Ferrer, K. Lynch, G. Neyens, and S. Sels, Analysis of counting data: Development of the SATLAS Python package, *Comput. Phys. Commun* **222**, 286 (2018).
- [29] V. A. Dzuba and V. V. Flambaum, Calculation of the hyperfine structure of Er and Fm, *Phys. Rev. A* **108**, 012823 (2023).
- [30] C. Froese Fischer, G. Gaigalas, P. Jönsson, and J. Bieroń,

- GRASP2018—A Fortran 95 version of the General Relativistic Atomic Structure Package, *Comput. Phys. Commun.* **237**, 184 (2019).
- [31] S. Fritzsche, Level structure and properties of open f-shell elements, *Atoms* **10**, 10.3390/atoms10010007 (2022).
- [32] R. Beerwerth and S. Fritzsche, Private communication (2019).
- [33] A. Barzakh, A. N. Andreyev, C. Raison, *et al.*, Large Shape Staggering in Neutron-Deficient Bi Isotopes, *Phys. Rev. Lett.* **127**, 192501 (2021).
- [34] J. Bieroń, L. Filippin, G. Gaigalas, M. Godefroid, P. Jönsson, and P. Pyykkö, Ab initio calculations of the hyperfine structure of zinc and evaluation of the nuclear quadrupole moment $Q(^{67}\text{Zn})$, *Phys. Rev. A* **97**, 062505 (2018).
- [35] S. Goriely, S. Hilaire, M. Girod, and S. Péru, First Gogny-Hartree-Fock-Bogoliubov Nuclear Mass Model, *Phys. Rev. Lett.* **102**, 242501 (2009).
- [36] S. Péru, S. Hilaire, S. Goriely, and M. Martini, Description of magnetic moments within the Gogny Hartree-Fock-Bogolyubov framework: Application to Hg isotopes, *Phys. Rev. C* **104**, 024328 (2021).
- [37] J. Sadoudi, T. Duguet, J. Meyer, and M. Bender, Skyrme functional from a three-body pseudopotential of second order in gradients: Formalism for central terms, *Phys. Rev. C* **88**, 064326 (2013).
- [38] R. Jodon, *Ajustements de fonctionnelles de Skyrme généralisées*, Ph.D. thesis, Université Claude Bernard - Lyon 1 (2014), Note that we use the variant that is called SLyMR1_{3b}.
- [39] B. Bally, B. Avez, M. Bender, and P.-H. Heenen, Beyond Mean-Field Calculations for Odd-Mass Nuclei, *Phys. Rev. Lett.* **113**, 162501 (2014).
- [40] B. Bally, G. Giacalone, and M. Bender, Structure of $^{128,129,130}\text{Xe}$ through multi-reference energy density functional calculations, *The European Physical Journal A* **58**, 187 (2022).
- [41] J. Lantis, A. Claessens, D. Münzberg, *et al.*, In-gas-jet laser spectroscopy of ^{254}No with JetRIS, *Phys. Rev. Res.* **6**, 023318 (2024).
- [42] J. Romans, A. Ajayakumar, M. Authier, F. Boumard, L. Caceres, J.-F. Cam, A. Claessens, S. Damoy, P. Delahaye, P. Desrues, *et al.*, First offline results from the S3 low-energy branch, *Atoms* **10**, 21 (2022).
- [43] P. Jönsson, M. Godefroid, G. Gaigalas, J. Ekman, J. Grumer, W. Li, J. Li, T. Brage, I. P. Grant, J. Bieroń, and C. Froese Fischer, An Introduction to Relativistic Theory as Implemented in GRASP, *Atoms* **11**, 7 (2022).
- [44] P. Jönsson, G. Gaigalas, C. Froese Fischer, J. Bieroń, I. P. Grant, T. Brage, J. Ekman, M. Godefroid, J. Grumer, J. Li, and W. Li, GRASP Manual for Users, *Atoms* **11**(4), 68 (2023).
- [45] A. Bohr and B. R. Mottelson, *Nuclear Structure. Volume II: Nuclear Deformations* (Benjamin, New York, Amsterdam, 1975).

Appendix A: Atomic theoretical methods — Calculations involving open f -shell systems are computationally very demanding, especially for excited states, therefore the focus in this investigations was on the ground state [Rn] $7s^25f^{12}3H_6$ GS. In particular, calculations involving MCDHF theory as implemented in GRASP18 [30] were performed for this work. In the standard formulation of the MCDHF theory, the function Ψ for a given state is represented as a linear combination of symmetry-adapted configuration state functions (CSFs),

$$\Psi(\Gamma\pi JM) = \sum_{i=1}^{N_{\text{CSF}}} c_i \Phi(\gamma_i \pi JM),$$

where J is the total electronic angular momentum, and M is its projection, π is the parity, γ_i represents the set of orbital occupancies and complete coupling tree of angular quantum numbers unambiguously specifying the i -th CSF, while Γ denotes all other information needed to uniquely describe the state [43]. A single reference calculation was performed on the ground state of Fm I. Five layers of correlation orbitals were generated by allowing single and double (SD) substitutions from the $5f$ and $7s$ valence orbitals. The maximum orbital angular momentum quantum number of the correlation orbitals was $\ell \leq 5$, which includes the g correlation orbitals to properly account for correlation effects between electrons in f shells. Afterwards, the relativistic configuration interaction RCI program was run to increase the active set of orbitals while keeping the orbital shapes fixed. In this stage, configuration state functions (CSFs) were generated by substituting orbitals with a principal quantum number $n \geq 4$. For this, a restriction of single and restricted double (SrD) substitutions was applied which means at most two electrons may be substituted with at minimum one belonging to the valence orbitals ($5f$, $7s$). In this stage, configuration state functions (CSFs) were generated by allowing substitutions of orbitals with principal quantum numbers $n \geq 4$. The substitutions were restricted to single and restricted double (SrD) excitations, meaning that at most two electrons could be substituted, with at least one electron coming from the valence orbitals ($5f$, $7s$).

The calculations were repeated for the lanthanide homologue Er I to demonstrate the predictive accuracy of our model. Good agreement was found between previous theory and experiment for Fm I and Er I, respectively. Convergence was demonstrated for the HFS parameter \mathcal{A} and at least weak convergence demonstrated for the HFS parameter \mathcal{B} in both Er I and Fm I. Nevertheless, further work might still be needed to demonstrate solid convergence for the \mathcal{B} HFS parameter. This stage of the calculation represents one of the largest MCDHF calculations of a single state. It required generating 16 million CSFs, reduced to 9 million after removing those CSFs which did not directly interact with the reference list [44].

Appendix B: Nuclear theoretical methods — The two microscopic nuclear structure models used to interpret the experimental findings are based on an energy density functional (EDF) framework. They both describe reasonably well the evolution of the mean squared charge radii of fermium isotopes [7]. One is using the Skyrme interaction SLyMR1 [37, 38], and the other the Gogny force D1M [35]. The latter model has also already been used to describe nuclear moments of californium isotopes [17]. In either case, the starting point is the calculation of energy surfaces of several self-consistently blocked one-quasiparticle (qp) configurations variationally optimized through the Hartree-Fock-Bogoliubov (HFB) method, followed by a selection of the configurations that are compatible with the experimentally deduced spin and parity. Contrary to the spectroscopic quadrupole moment, the magnetic moment of a deformed nucleus cannot be directly calculated as the expectation value of the magnetic dipole operator of a qp configuration. Instead, the axial HFB calculations with D1M are mapped on the unified model [45] as described in Ref. [36]. In addition, to approximately take configuration mixing into account, the D1M results average over deformation, as described in Ref. [33]. By contrast, for SLyMR1 calculations, a full configuration mixing of symmetry-restored reference states is performed within a Multi-Reference Energy Density Functional (MREDF) framework including triaxial shapes as described in Ref. [40]. Finally, we mention that the SLyMR1 results for magnetic moments are calculated with bare g factors, whereas for the D1M results the spin contributions are quenched with a factor of 0.75 [36].